

RESEARCH ARTICLE

View Article Online

View Journal | View Issue

Cite this: *Inorg. Chem. Front.*, 2023, 10, 3273A new 0D–2D CsPbBr₃–Co₃O₄ heterostructure photocatalyst with efficient charge separation for photocatalytic CO₂ reduction†Xin Zhong,^{‡a} Xinmeng Liang,^{‡a} Xinyu Lin,^a Jin Wang,^{ID} ^{*a,b}
Malik Zeeshan Shahid^{ID} ^{*a} and Zhengquan Li^{ID} ^{*a,b}

The effective spatial separation of photogenerated charge carriers is essential for realizing efficient CO₂ conversion. Herein, a new CsPbBr₃–Co₃O₄ heterostructure photocatalyst was rationally developed for photocatalytic CO₂ reduction. A facile synthetic strategy based on electrostatic interactions was utilized. The results revealed that the CsPbBr₃–Co₃O₄ hybrid exhibited a boosted evolution rate of 64.6 μmol g^{−1} h^{−1} (CO: 35.40 μmol g^{−1} h^{−1}; CH₄: 29.2 μmol g^{−1} h^{−1}) with an electron consumption rate (*R*_{electron}) of 304.4 μmol g^{−1} h^{−1}, surpassing pristine CsPbBr₃ or Co₃O₄. The high activity mainly arises from efficient charge separation and the directional transfer of electrons from CsPbBr₃ to Co₃O₄ via an intimately coupled heterointerface. Notably, the surface features (derived from the unique morphology) expedited the CO₂ adsorption and accumulation of electrons at the Co₃O₄ site which ultimately facilitated the conversion of CO₂ over the CsPbBr₃–Co₃O₄ composite. This approach provides a strategy to design and modulate highly active metal oxide and perovskite-based photocatalysts and presents great potential for constructing a heterointerface for CO₂ reduction.

Received 21st March 2023,

Accepted 17th April 2023

DOI: 10.1039/d3qi00527e

rsc.li/frontiers-inorganic

1. Introduction

The daily consumption of fossil fuels results in the emission of CO₂, causing universal environmental and energy issues.^{1–4} Fixation of CO₂ into value-added products such as CO, CH₄, HCOOH, CH₃OH, *etc.* via solar-driven catalysis, also known as artificial photosynthesis, is a clean and sustainable solution.^{5–7} However, it is challenging and suffers low conversion efficiency due to the high thermodynamic stability of CO₂ molecules and the need for multi-electron transfer.^{8,9} Recently, instead of using single-component photocatalysts, research efforts have been diverted to designing their low-cost heterostructures. Many materials, such as C₃N₄,^{10,11} ZrO₂,¹² TiO₂,¹³ Ta₂O₅,¹⁴ Nb₂O₅,¹⁵ metal sulfides,¹⁶ metal-organic frameworks,¹⁷ metal complexes,⁷ single-atom catalysts,¹⁸

MXenes,¹⁹ conducting polymers,²⁰ metal halide perovskites,^{6,21} *etc.*, have been reported aiming at activity enhancement via optimizing the light-harvesting and charge carrier kinetics. However, the search for a more effective candidate photocatalyst has not stopped.

Among numerous materials, all inorganic metal halide perovskites, particularly cesium lead-bromide perovskite quantum dots (CsPbBr₃ QDs), are extremely competitive photocatalysts for CO₂ reduction.^{1,6,22,23} This is owing to their suitable energy band structure, small size, defect tolerance, and large carrier mobility as compared to other inorganic metal halide family members, *e.g.* CsPbCl₃ and CsPbI₃.^{1,6,24–43} However, pristine CsPbBr₃ QDs suffer from instability and rapid recombination of electron-hole (e[−]–h⁺) pairs, leading to low activity. To address this issue, Xu *et al.* first utilized the CsPbBr₃ QDs/graphene composite for the photocatalytic reduction of CO₂.⁴³ After that, several efforts were devoted to enhance its performance. For instance, our group designed CsPbBr₃ QDs/Bi₂WO₆³⁸ and CsPbBr₃ QDs coupled with covalent triazine frameworks,³⁶ and both exhibited enhanced charge separation and led to improved CO₂ photoreduction. But the produced gas was mainly CO and only a minimum of CH₄ was detected. This was possibly due to the lack of sufficient accumulation of reductive electrons at catalytic sites.

^aKey Laboratory of the Ministry of Education for Advanced Catalysis Materials, Zhejiang Normal University, Jinhua, Zhejiang 321004, P. R. China.

E-mail: zqli@zjnu.edu.cn, zeeshan-nano@zjnu.edu.cn, wangjin@zjnu.edu.cn

^bZhejiang Institute of Optoelectronics, Zhejiang Normal University, Jinhua, Zhejiang 321004, P. R. China

†Electronic supplementary information (ESI) available. See DOI: <https://doi.org/10.1039/d3qi00527e>

‡These authors contributed equally.

So, we further our research to find some suitable materials which can form an intimately coupled interface with CsPbBr₃ QDs and enable efficient photocatalysis to generate both CO and CH₄, thereby overcoming the intrinsic issues of CsPbBr₃ QDs.

We found that the transition metal oxide photocatalyst cobalt oxide (Co₃O₄) is an ideal non-precious catalyst for CO₂ reduction as it exhibits suitable band alignment, efficient charge-carrier flux capability, and chemical/thermodynamic stability.^{44–52} However, the typical single component Co₃O₄ may suffer limited preservation of reductive electrons as well as hindered spatial separation of e[−]–h⁺ pairs. Multiple morphologies have been constructed to meet such limitations, such as nanorods,⁵³ ultrathin nanosheets,⁵⁴ nanofibers,⁵⁵ hollow dodecahedra,⁴⁸ porous structures,⁵⁶ and mesoporous two-dimensional (2D) hexagonal nanoplatelets (HPs) with various facets and catalytically active sites.^{45,57} For example, Gao *et al.* first developed [112] facet-rich Co₃O₄ HPs,⁵² and then later on Zhu *et al.* constructed the Co₃O₄/g-C₃N₄ (2D/2D) hybrid,⁵⁷ both intended to facilitate the separation of charge carriers for photocatalytic CO₂ conversion. Inspiringly, we intend to develop a high-performance Co₃O₄ heterostructure catalyst by simultaneously promoting charge separation and preserving the reductive electrons. It is widely accepted that constructing a heterostructure is efficient for channelizing and accelerating the separation and transfer of e[−]–h⁺ pairs *via* a strongly coupled interface developed through proper band alignment and work functions (Φ).^{47,58–61} Therefore, constructing a hybrid between CsPbBr₃ QDs and Co₃O₄ HPs probably can result in an improved photocatalytic performance toward CO₂ reduction. To the best of our knowledge, there is no report on the fabrication of CsPbBr₃ QDs on Co₃O₄ HPs, and it is desirable to design and construct a new heterostructure based on CsPbBr₃ QDs and Co₃O₄ HPs for CO₂ photoreduction.

Herein, a CsPbBr₃–Co₃O₄ heterojunction photocatalyst is developed *via* electrostatic self-assembly between Co₃O₄ HPs and CsPbBr₃ QDs for photocatalytic CO₂ reduction. Investigations confirmed the successful formation of the CsPbBr₃–Co₃O₄ hybrid. Diverse physicochemical and optoelectronic characterization studies revealed that: (i) Co₃O₄ HPs acted as a supporting matrix to collect electrons from CsPbBr₃, rendering electron localization; (ii) the CsPbBr₃–Co₃O₄ hybrid exhibited compact heterointerfaces, facilitating robust charge separation with hampered e[−]–h⁺ pair recombination; (iii) the Co₃O₄ side offers numerous mesopores and catalytic sites, which facilitate the better capturing and activation of CO₂ molecules. Consequently, CsPbBr₃–Co₃O₄ showed improved activity for the generation of CO and CH₄, with an evolving rate of 35.40 and 29.2 $\mu\text{mol g}^{-1} \text{h}^{-1}$, respectively, surpassing their pristine counterparts *i.e.*, CsPbBr₃ QDs and Co₃O₄ HPs, as well as recent state-of-the-art photocatalysts (Table S1†). This work highlights the rational design of new metal halide perovskite-based photocatalysts and addresses the critical issues regarding charge carrier kinetics to realize efficient solar-driven CO₂ conversion.

2. Experimental section

2.1. Synthesis of CsPbBr₃ QDs

To obtain CsPbBr₃ QDs, the reported method was followed (see also in Fig. S1†).⁶² Briefly, for the Cs-OA stock solution, 0.2 g of cesium carbonate (Cs₂CO₃), 10 mL of octadecene (ODE, C₁₈H₃₆), and 0.6 mL of oleic acid (OA, C₁₈H₃₄O₂) were loaded into a three-necked round bottom flask. Under Ar flow, the temperature was increased to 120 °C and a clear light-yellow solution was obtained. The temperature was increased to 150 °C just before the hot injection. For the Pb stock solution, 0.1380 g of lead bromide (PbBr₂) and 10 mL of ODE were added into a 50 mL three-necked round bottom flask, under Ar flow, the temperature was increased to 120 °C to get a white turbid liquid and maintained it for 30 min. Next, the temperature was further increased to 165 °C, and 1.5 mL OA and 1.1 mL OAm were added to the Pb stocks. When a yellow homogeneous solution was obtained, 0.8 mL of the Cs-stock solution was swiftly injected into it. After 5 s, the mixture was immediately cooled down using an ice-water bath. The original solution was directly centrifuged at 8000 rpm for 5 min and further washed with ethyl acetate and isopropanol to remove the organic residue. Finally, the CsPbBr₃ QDs collected and stored in *n*-hexane are added in an equal volume.

2.2. Preparation of Co₃O₄ HPs

To obtain Co₃O₄ HPs, the previously reported method was modified (see also in Fig. S2†).⁵² Firstly, β -Co(OH)₂ precipitates were prepared. 0.2379 g (5 mmol) of cobalt chloride hexahydrate (CoCl₂·6H₂O), 1.6823 g (60 mmol) of cyclohexamethylenetetramine (urotropine), 180 mL of deionized water and 20 mL of ethanol were added into a beaker under stirring. The mixture was heated in an oil bath to 90 °C for 1 h to obtain a pink solution. After cooling it to an ambient temperature, it was centrifuged at 9000 rpm for 15 min to obtain a pink precipitate of β -Co(OH)₂. Subsequently, 50 mL of deionized water and 50 mL of ethanol were added, and the β -Co(OH)₂ precipitate was redispersed by ultrasonication. The sample was collected by centrifuging at 9000 rpm for 15 min. This operation was repeated 3 times. The obtained precipitate was freeze-dried under vacuum for 6 hours. Finally, the precipitate was transferred into a cuboid crucible and put into a muffle furnace for calcination at 400 °C for 3 h to obtain a black powder of Co₃O₄ HPs.

2.3. Synthesis of the CsPbBr₃–Co₃O₄ heterostructure

The CsPbBr₃–Co₃O₄ heterostructure was prepared using a solution-processed approach at room temperature. First, 0.5 mg of the Co₃O₄ HP powder was dispersed into 250 μL of ethanol under uninterrupted stirring. Second, 400 μL (2 mg) of CsPbBr₃ QDs were dispersed into 5 mL of ethyl acetate. Third, the CsPbBr₃ QD solution was swiftly added into the solution of Co₃O₄ HPs and mechanically stirred at room temperature in the dark for 30 min. Finally, the mixture was ultrasonicated for another 30 min under ambient conditions. The obtained solution was centrifuged at 8000 rpm for 5 min, and the precipitate

was vacuum dried overnight at 45 °C to obtain the CsPbBr₃-Co₃O₄ heterojunction. This synthesis was performed with an optimum mass ratio (Co₃O₄ HPs:CsPbBr₃ QDs) *i.e.*, 1:4, and a similar method was followed to obtain various mass ratios such as 1:1, 1:2, 1:8, and 1:16. Step by step addition of Co₃O₄ HPs and CsPbBr₃ QDs as well as the formation process of the CsPbBr₃-Co₃O₄ heterojunction are also picturized and described in Fig. S3.† The details of all materials and other characterization studies for physicochemical and optoelectronic properties are provided in the ESI.†

3. Results and discussion

3.1. Illustration of the synthesis process and verification of the heterostructure formation

Firstly, CsPbBr₃ QDs (0D) was precisely prepared *via* a typical hot-injection method (Fig. S1†).⁶² Subsequently, Co₃O₄ HPs (2D) holding rich facets [112] were synthesized through the calcination of brucite-like cobalt hydroxide β-Co(OH)₂ precipitates (Fig. S2†).⁵² Finally, to obtain a 0D/2D CsPbBr₃-Co₃O₄ heterojunction, their mixture at an optimum mass ratio 4:1 (CsPbBr₃ QDs:Co₃O₄ HPs) was exclusively stirred in a solution of ethyl acetate and ethanol at room temperature (Scheme 1, see details in Fig. S3†). The tactic used here is based on the Coulomb electrostatic assembly which enables the incorporation of CsPbBr₃ QDs and Co₃O₄ HPs. The zeta potentials of pristine CsPbBr₃ QDs and Co₃O₄ HPs are 4.80 mV and -3.10 mV, respectively (Fig. S4†), which indicates oppositely charged surfaces encounter electrostatic attractions, resulting in the formation of CsPbBr₃-Co₃O₄. Such a kind of electrostatic self-assembly would possess a strong heterointerface, beneficial for interfacial charge transfer.⁶³

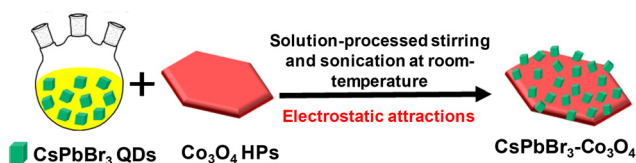
To confirm the successful formation of the CsPbBr₃-Co₃O₄ hybrid, powder X-ray diffraction (XRD) was first conducted (Fig. 1a). Pristine CsPbBr₃ QDs exhibit a typical cubic-phase (JCPDS card, No. 75-0412). Meanwhile, pristine Co₃O₄ HPs show diffraction patterns associated with the face-centred cubic phase of the spinel Co₃O₄ (JCPDS card No. 74-1657). Notably, strong signals of all peaks emerged and co-existed in the CsPbBr₃-Co₃O₄ hybrid, illustrating the successful formation of the heterojunction and the crystal phases were well maintained. To confirm this claim, nitrogen adsorption-desorption analysis was performed (Table S2†). It can be seen that after the precise formation of the heterojunction, the pore size and pore volume were reduced from 31.3 nm to 21.21 nm

and 0.1325 cm³ g⁻¹ to 0.0266 cm³ g⁻¹ respectively. In addition, the BET surface area also decreased from 16.9 m² g⁻¹ to 5.016 m² g⁻¹. This result indicates that the mesopores of Co₃O₄ were occupied by CsPbBr₃ QDs. Besides in the XRD, an exclusive color transformation was observed from black (Co₃O₄-HPs, Fig. 1b) and bright yellow (CsPbBr₃ QDs, Fig. 1c) to dark grey (CsPbBr₃-Co₃O₄, Fig. 1d). In addition, under ultra-violet irradiation, the CsPbBr₃-Co₃O₄ heterojunction demonstrated a dark green fluorescence in comparison with the bright green fluorescence of CsPbBr₃ QDs (Fig. S5†). Such color transformations further endorse that the heterojunction was constructed successfully in a well-controlled manner *via* a current facile strategy.

Transmission electron microscopy (TEM) and scanning electron microscopy (SEM) analysis further confirmed the formation of the heterojunction. CsPbBr₃ QDs exhibited an average size of about 12 nm (Fig. 1e and inset), whereas Co₃O₄ exhibits a hexagonal platelet-like structure with lateral sizes of ~4 ± 1 μm, and a thickness of about ~50 ± 10 nm, a dominant facet (112), and mesopores (Fig. 1f and inset). Importantly, after incorporating CsPbBr₃ QDs into Co₃O₄ HPs, several facts were noticed. (i) Both CsPbBr₃ QDs and Co₃O₄ HPs co-existed with well-defined morphologies, and their sizes were preserved without any further ripening, verifying that the synthesis was well-controlled (Fig. 1g). (ii) Besides electrostatic interactions, the huge surface energy of CsPbBr₃ QDs could drive its face-to-face attaching to Co₃O₄ HPs. (iii) CsPbBr₃ QDs were well dispersed (denoted by yellow circles) all over Co₃O₄ HPs, both on the inner side (Fig. 1g and inset) and on the boundary sides (Fig. 1h) and this would facilitate the formation of a rich heterointerface. (iv) Even though most of the mesopores were occupied by CsPbBr₃ QDs, still many mesopores could be observed as denoted by the marked area in green (Fig. 1g, h, and the inset).

Such accessible mesopores are not only beneficial for supporting CO₂ adsorption but also facilitate the exposure of the innermost lattice surfaces for the rapid transfer of photo-induced e⁻ to the outermost active surface sites.^{52,57} More clear evidence regarding the formation of the heterointerface was collected *via* high-resolution TEM analysis (HRTEM, Fig. 1i and j). The spacing in the lattice fringes was found to match well with both constituents, that is, 0.58 nm and 0.285 nm being the corresponding planes of CsPbBr₃ and Co₃O₄ respectively (Fig. 1j). Accordingly, the HAADF and energy dispersive X-ray (EDX) mapping analysis depicts the precise incorporation and distribution of all elements including Cs, Pb, Br, Co, and O in the CsPbBr₃-Co₃O₄ heterojunction (Fig. 1k-p). The above results are in-line with the XRD and TEM analysis, validating the formation of the heterojunction with finely dispersed CsPbBr₃ QDs on the support matrix of Co₃O₄ HPs.

Next, surface chemical states and interfacial interaction in the CsPbBr₃-Co₃O₄ heterojunction were evaluated *via* high-resolution X-ray photoelectron spectroscopy (XPS) of Cs 3d, Pb 4f, Br 3d, Co 2p, and O 1s. It is noteworthy that, in comparison with CsPbBr₃ QDs, the binding energy of Cs 3d (Fig. 2a), Pb 4f



Scheme 1 Illustration for the formation of the CsPbBr₃-Co₃O₄ heterojunction *via* electrostatic attraction.

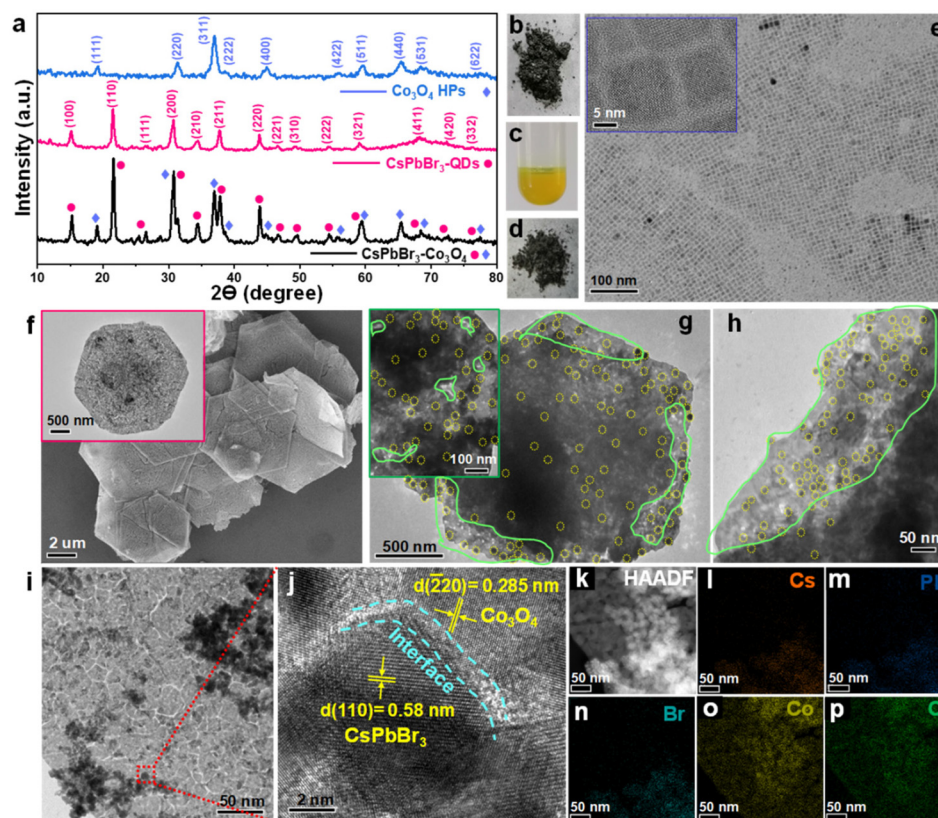


Fig. 1 (a) Comparison of the XRD pattern for the as-prepared products within the 2 theta range 10° – 80° , where pink circles and blue diamonds denote the corresponding peaks in the Co_3O_4 – CsPbBr_3 heterojunction originating from pristine products. Exclusive color transformation of the as-synthesized products where (b) Co_3O_4 HPs black, (c) CsPbBr_3 QDs bright yellow, and (d) CsPbBr_3 – Co_3O_4 dark grey. (e) The TEM image of pristine CsPbBr_3 QDs and the corresponding inset with high magnification. (f) The SEM image with low magnification and the inset is the TEM image for a single particle of Co_3O_4 HPs showing a hexagonal platelet-like morphology. (g) The TEM image of a Co_3O_4 – CsPbBr_3 heterojunction and the corresponding inset which was captured from the central side of a random particle and (h) the image taken from the boundary side. Finely dispersed CsPbBr_3 QDs are denoted with yellow circles and the pores are denoted with green marked areas. (i) and (j) HRTEM images, and (k–p) HAADF and EDX mapping results for the Co_3O_4 – CsPbBr_3 heterojunction.

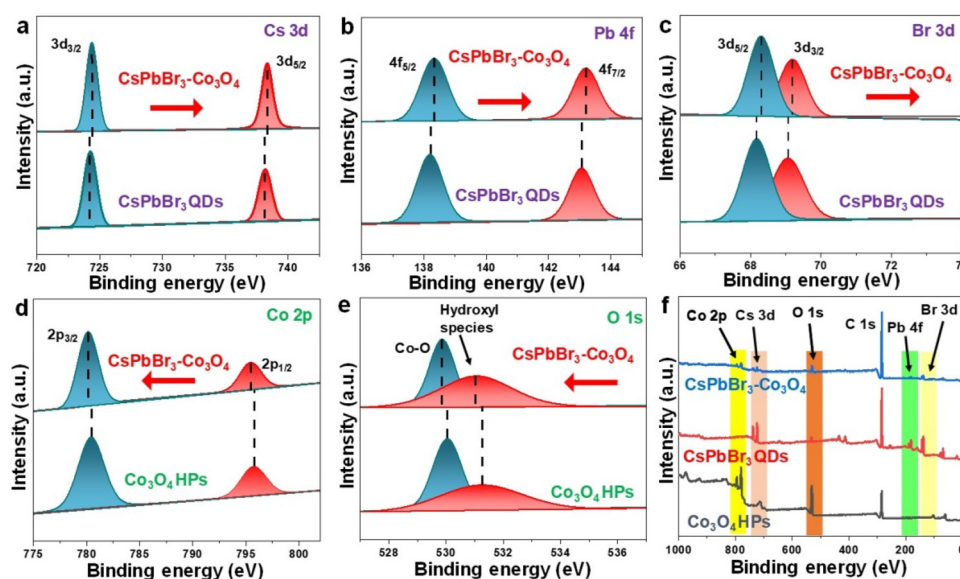


Fig. 2 Comparative representation of high-resolution XPS spectra for (a) Cs 3d, (b) Pb 4f, (c) Br 3d, (d) Co 2p, and (e) O 1s in all the synthesized products. (f) The XPS survey spectrum highlights the co-existence of CsPbBr_3 QDs and Co_3O_4 HPs in the CsPbBr_3 – Co_3O_4 heterojunction.

(Fig. 2b), and Br 3d (Fig. 2c) faced a positive shift in the heterojunction. This result strongly endorsed the close interfacial contact between QDs and HPs. Meanwhile, the XPS of Co 2p spectra signals were comparatively examined for CsPbBr₃-Co₃O₄ and Co₃O₄ HPs (Fig. 2d), where two binding energy values at 796 ± 0.2 eV and 780 ± 0.2 eV fit to Co 2p_{1/2} and Co 2p_{3/2}, respectively, which normally attributed to two main regions *i.e.*, Co²⁺ and Co³⁺.⁴⁴ As is known the theoretical value for the atomic ratio Co²⁺/Co³⁺ is 0.5 (*i.e.*, perfect Co₃O₄), but this value may increase in the presence of surface defects or oxygen vacancies (OVs).⁴⁴ Herein, no signal corresponding to defects in O 1s spectra (Fig. 2e) was found, which means that Co₃O₄ synthesized here is perfect and in an equally balanced state. Notably, the absence of OVs also indicates that the high crystallinity of Co₃O₄ was maintained after forming the CsPbBr₃-Co₃O₄ heterojunction. Meanwhile, a slight negative shift towards the lower binding energy was observed, demonstrating the interaction between Co₃O₄ and CsPbBr₃ (Fig. 2d). Moreover, relative O 1s spectra disclosed two main peaks that fit with the hydroxyl species and Co-O bond respectively. In addition, the obvious co-existence of CsPbBr₃ QDs and Co₃O₄ HPs is supported through the XPS survey spectrum (Fig. 2f). All the characteristic peaks are assigned to Cs, Pb, Br, Co, and O (highlighted with bars), affirming the formation of the CsPbBr₃-Co₃O₄ heterojunction.

3.2. Investigation of the photocatalytic activity for CO₂ reduction

The activity of the as-synthesized CsPbBr₃-Co₃O₄ heterojunction for CO₂ photocatalytic reduction is evaluated under the solid-gas environment using 50 μ L of water as the proton source (see details in the ESI section 1.3†).^{36,38,63} In particular, no sacrificial agent was used, and visible light was irradiated during photocatalysis. As shown in Fig. 3a, the pristine components only can produce limited CO and negligible CH₄, calculated to be 14.23 and 0.39 (for CsPbBr₃ QDs) and 9.52 and 0.46 (for Co₃O₄ HPs) μ mol g⁻¹ h⁻¹, respectively. Notably, the CsPbBr₃-Co₃O₄ heterojunction delivered an enhanced performance for the evolution of CO and CH₄, which is 35.40 and 29.2 μ mol g⁻¹ h⁻¹, respectively. The corresponding electron consumption rate (R_{electron} , see the formula in Table S2†) was found to be 304.4 μ mol g⁻¹ h⁻¹, which is 9.51 and 13.4 fold larger than that of pristine CsPbBr₃ QDs and Co₃O₄ HPs,

respectively. The maximum cumulative production of CO and CH₄ after a 6-hour reaction was 211.58 and 175.31 μ mol g⁻¹, respectively (Fig. S6†). The current performance of the CsPbBr₃-Co₃O₄ heterojunction was found to be exceeding that of the pristine counter components as well as recent state-of-the-art photocatalysts (Table S1†). Moreover, altering the dosage ratio of Co₃O₄:CsPbBr₃ in the heterojunction could greatly influence the activity, for instance, the upper limit of gases was only reached with an optimum mass ratio of 1:4 (Fig. S7†).

More and/or less dosage of CsPbBr₃ than the optimum value in the heterojunction is not conducive to producing CO and CH₄ in high yields, maybe due to the insufficient amount and/or blockage of active sites respectively, and this phenomenon was found to be consistent with the literature.³⁸ Additionally, control experiments were performed to confirm the origin of CO, and CH₄ during photocatalysis (Fig. 3b). First, under an argon atmosphere, traces of CO or CH₄ was found, which shows that feed-stock CO₂ is necessary to run the photocatalytic reduction reaction.^{36,38,63} Second, nothing was detected under the dark conditions, which again confirms light irradiation is required to obtain CO and CH₄ from the reduction of CO₂. Finally, the optimum result could only be achieved using the CsPbBr₃-Co₃O₄ heterojunction with a mass ratio of 1:4 as the photocatalyst, CO₂ gas as the feedstock, and solar light illumination ($\lambda > 400$ nm). To further verify the origin of the carbon source of the photo-generated CO and CH₄, ¹³CO₂ isotope labelling was performed and the GC-MS result is displayed in Fig. S8.† Evidently, the signals belonging to ¹³CO (*m/z* 29) and ¹³CH₄ (*m/z* 17) are derived from ¹³CO₂, validating that CO₂ feedstock is the actual carbon source. Likewise, the oxidation of water to oxygen further validates the continuous supply of protons during CO₂ conversion (Fig. S9†). Furthermore, the CsPbBr₃-Co₃O₄ heterojunction can remain stable during the consecutive 5 cycles (Fig. 3c). The morphological and structural characteristics of the CsPbBr₃-Co₃O₄ heterojunction are well-maintained after photocatalysis (Fig. S10a and S10b†).

3.3. Unveiling of the origins for improved activity

The origins of the possible enhanced activity were investigated and have been described systematically. The CO₂ adsorption

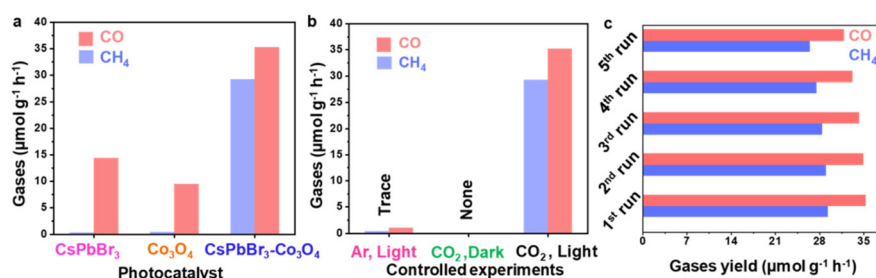


Fig. 3 (a) A comparative depiction of the catalytic activity in terms of the produced gases CO and CH₄ using the as-synthesized CsPbBr₃ QDs, Co₃O₄ HPs, and CsPbBr₃-Co₃O₄ heterojunction. (b) Controlled experiments were performed under different reaction conditions to produce CO and CH₄ to examine the origin of the evolved gases. (c) Stability test of the CsPbBr₃-Co₃O₄ heterojunction for 5 consecutive cycles.

on the surface of the photocatalyst is a primary step that would further govern its activation and conversion. And it is well-known that CsPbBr₃ QDs have a large surface area and are capable of adsorbing more CO₂ on their surface.^{32,43} As verified by the TEM analysis, the size of CsPbBr₃ QDs remained unchanged after forming a hybrid with Co₃O₄ HPs, indicating that it would exhibit similar CO₂ adsorption activity on its surface. Likewise, Co₃O₄ HPs also possess numerous adsorption sites derived from their structural mesopores. Although most of the mesopores are occupied by CsPbBr₃ QDs (Fig. S11 and Table S2†), additional porosities are still accessible in the heterojunction (as shown in the green marked area in Fig. 1g and h). These porosities would actively endure the CO₂ adsorption.^{52,57}

As the light absorption range is a key factor in solar-driven catalysis, to investigate the light-harvesting ability of the as-prepared components, diffuse reflectance spectra (DRS) were recorded. Both CsPbBr₃ QDs and Co₃O₄ HPs show a strong visible light response within the wavelength range of 400–600 nm, and their corresponding energy band gaps (E_g), determined to be 2.36 eV and 2.31 eV, respectively, are well-consistent with the literature (Fig. 4a and b and corresponding insets).^{38,52} Where; E_g is estimated through Tauc plots using the equation $ah\nu = A(h\nu - E_g)^n$ (see details in section 1.5 of the ESI†). It is to be noted that $E_{1g} = 1.83$ eV is attributed to the $O^{2-} \rightarrow Co^{3+}$ excitation and is not a real energy bandgap of Co₃O₄ HPs.^{52,64–66} The enhanced light absorption ability of both components in the CsPbBr₃–Co₃O₄ heterojunction supports its higher catalytic activity. Moreover, the valence and conduction band positions (E_{VB} and E_{CB}) strongly define the thermodynamic feasibility of CO₂ reduction reactions. According to the reported results, the E_{CB} of Co₃O₄ and CsPbBr₃ are -0.64 eV⁵² and -0.99 eV,³⁶ respectively, and cor-

respondingly, the calculated E_{VB} for Co₃O₄ HPs and CsPbBr₃ QDs are 1.67 eV and 1.37 eV, respectively. Hence, the consequent CsPbBr₃–Co₃O₄ heterojunction possess efficient light harvesting ability with staggered band alignment as depicted in Fig. 5a, further endorsing an uninterrupted CO₂ conversion.

The rapid radiative recombination of photoinduced e^- – h^+ pairs in pristine CsPbBr₃ QDs can lead to low CO₂ conversion efficiency.²⁴ This was exclusively observed, where the intense photoluminescence (PL) spectra signal for pristine CsPbBr₃ QDs (Fig. 4c) confirmed its low catalytic activity. However, after immobilizing CsPbBr₃ QDs on Co₃O₄ HPs, the results dramatically changed towards low PL intensity, identifying the significantly hindered recombination of e^- – h^+ pairs over the CsPbBr₃–Co₃O₄ heterojunction (Fig. 4c and Fig. S12†). This finding matched well with the enhanced photocatalytic performance. This also means, combining such photocatalysts can substantially quench the radiative recombination of the metal halide perovskite, thereby exhibiting high activity. Likewise, to investigate the charge transfer kinetics, PL decay was also inquired *via* time-resolved photoluminescence spectroscopy (TRPL), curves were fitted with a bi-exponential function, Table S3† and Fig. 4d). The CsPbBr₃–Co₃O₄ heterojunction demonstrated a shorter lifetime ($\tau_{avg} = 45.04$ ns) in comparison with pristine CsPbBr₃ QDs ($\tau_{avg} = 47.43$ ns). This outcome further verified the restrained recombination of e^- – h^+ pairs and their efficient separation in the CsPbBr₃–Co₃O₄ hybrid. Besides charge recombination, charge transfer kinetics and their directional transfer are decisive to realize an improved CO₂ conversion.^{61,67,68} Therefore, these were investigated for the CsPbBr₃–Co₃O₄ heterojunction through electrochemical impedance spectroscopy (EIS) and transient photocurrent responses (TPR). The smallest arc radius was seen for the CsPbBr₃–Co₃O₄ heterojunction followed by CsPbBr₃ QDs

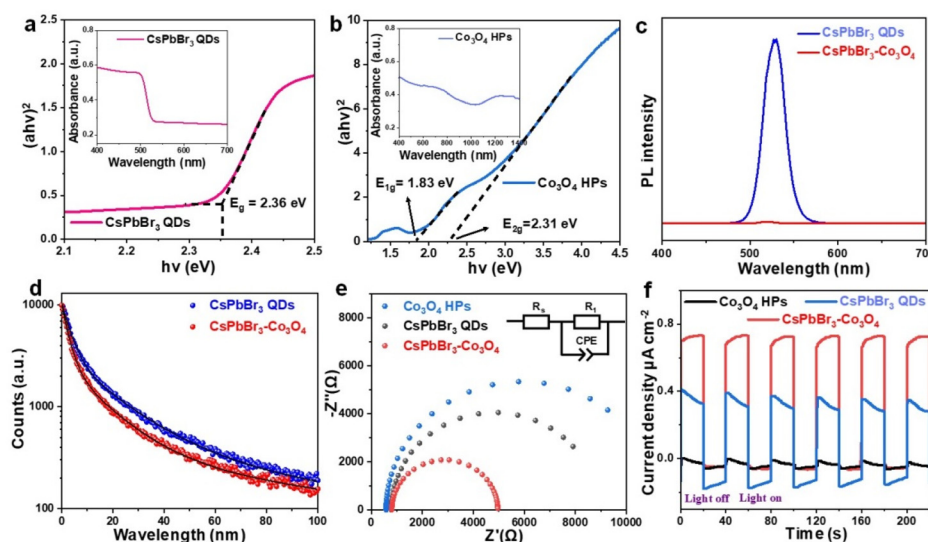


Fig. 4 Tauc plots for energy bands and their corresponding insets depicting the diffuse reflectance spectra curves for (a) CsPbBr₃ QDs and (b) Co₃O₄ HPs. (c) Steady-state photoluminescence spectra, and (d) time-resolved photoluminescence spectroscopy of CsPbBr₃ QDs and the CsPbBr₃–Co₃O₄ heterojunction. (e) Electrochemical impedance spectra and (f) transient photocurrent spectra of all the as-prepared products.

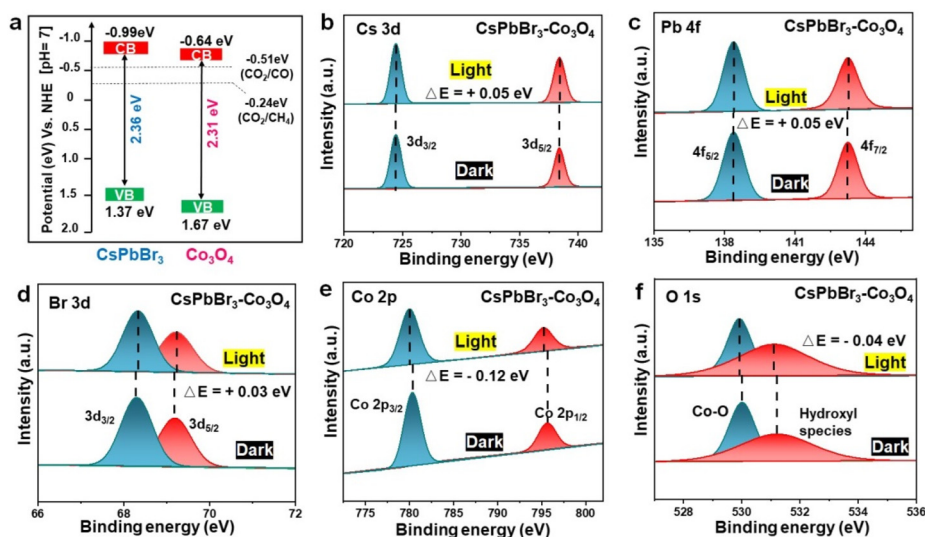


Fig. 5 (a) Redox potentials and band alignment of the CsPbBr₃-Co₃O₄ heterojunction. The *in situ* XPS analysis of (b) Cs 3d, (c) Pb 4f, (d) Br 3d, (e) Co 2p, and (f) O 1s, showing the electron-rich and electron-deficient sides in the CsPbBr₃-Co₃O₄ heterojunction.

and Co₃O₄ HPs (Fig. 4e). The markedly inhibited resistance in CsPbBr₃-Co₃O₄ would promote charge transfer. Likewise, the CsPbBr₃-Co₃O₄ shows the highest photocurrent with high repeatability (Fig. 4f). This result further supports the accelerated separation of e⁻-h⁺ pairs as well as highlights that an accessible route builds up (*i.e.*, heterointerface) by decorating CsPbBr₃ QDs on Co₃O₄ HPs.

3.4. Uncovering charge redistribution on the intimately coupled heterointerface and the corresponding catalytic mechanism

To further shed light on the interfacial charge-carrier flux, and their transfer route, particularly the accumulation of reductive electrons, the *in situ* XPS spectra were conducted under dark and visible light irradiation, respectively. As can be seen, the binding energies corresponding to Cs 3d, Pb 4f, and Br 3d exclusively underwent a positive shift (Fig. 5a-c) under light, which demonstrates a decrease of the electron density in the CsPbBr₃ side. In the meantime, the peak attributed to Co 2p and O 1s shifted to lower binding energy, suggesting an increased electron density at the Co₃O₄ side (Fig. 5e and f). Such patterns verify the continuous transfer of photoinduced electrons from CsPbBr₃ to Co₃O₄. In other words, Co₃O₄ plays a role as a supporting matrix to evoke and gather electrons from CsPbBr₃ QDs, allowing electron localization on the active surface of Co₃O₄. At the same time, an uninterrupted separation of e⁻-h⁺ pairs occurs in CsPbBr₃ owing to the significantly improved light harvesting ability and abundant exposed surface. Therefore, the electron-rich and electron-deficient phenomena occur simultaneously to balance the electron redistribution in the CsPbBr₃-Co₃O₄ heterojunction. Notably, except for the negative shift in O 1s spectra (Fig. 5f), no new peak belonging to OV appeared, validating the structural permanence of Co₃O₄ in the heterojunction.

Furthermore, the work function (Φ) is another pivotal factor for charge carrier kinetics, particularly at the heterointerfaces. The Φ for CsPbBr₃ QDs and Co₃O₄ HPs are 4.39 eV and 5.74 eV respectively.^{33,52} So, a larger Φ value of Co₃O₄ refers to its lower Fermi level (E_f) than that of CsPbBr₃, implying that the flow of electrons is from CsPbBr₃ to Co₃O₄ which is consistent with the outcomes of *in situ* XPS. This would hasten the extraction of reductive electrons from CsPbBr₃ to Co₃O₄, thus suppressing the recombination of e⁻-h⁺ pairs. In a word, CsPbBr₃ facilitated the rapid and continuous electron transfer *via* shorter diffusion pathways due to the size effect, and Co₃O₄ spontaneously accepted the electrons and accumulated on its active surface to exclusively participate in CO₂ reduction under the irradiation of solar light.

Based on the above results, the proposed CO₂ photoreduction mechanism over the CsPbBr₃-Co₃O₄ hybrid has been described. As illustrated in Fig. 6a, CsPbBr₃ and Co₃O₄ in the heterojunction have a staggered band alignment (type-II). In addition, the CsPbBr₃-Co₃O₄ heterojunction holds enough

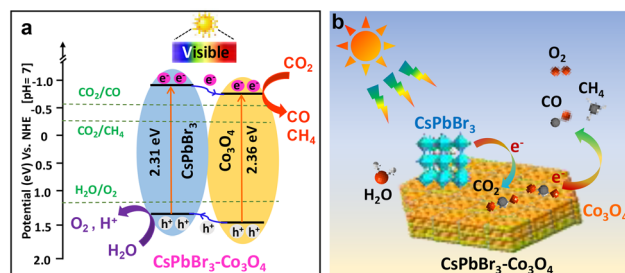


Fig. 6 (a) Photoexcited charge separation and their transfer route over the CsPbBr₃-Co₃O₄ heterojunction under visible light irradiation. (b) Schematic diagram depicting the continuous flow of electrons from CsPbBr₃ towards Co₃O₄ enabling the photocatalytic conversion of CO₂.

negative CB and positive VB potentials to reduce CO₂ and oxidize water, respectively. Under light irradiation, electrons and holes can be generated in both CsPbBr₃ and Co₃O₄. Subsequently, the photoinduced electrons are transferred from CB of CsPbBr₃ to CB of Co₃O₄ (Fig. 6b), causing electron localization at the Co₃O₄ side, making it suitable to conduct the CO₂ reduction reaction (as mentioned earlier in the *in situ* XPS analysis section). In the meantime, holes are transported in opposite directions *i.e.*, from VB of Co₃O₄ to VB of CsPbBr₃, building a hole-rich CsPbBr₃ side, favourable for oxidizing H₂O to O₂ and H⁺. Accordingly, the breaking of C=O bonds in CO₂ occurred at the electron-rich Co₃O₄ side, where the coupling of electron and protons took place, for instance, 2e⁻ and 8e⁻ get coupled with 2H⁺ and 8H⁺ to produce CO and CH₄, respectively, as presented in eqn (1) and (2). Thus, the effective charge separation enables the uninterrupted electron-proton integrative reaction to realize highly efficient CO₂ photocatalytic reduction over the CsPbBr₃-Co₃O₄ heterojunction.



4. Conclusions

In conclusion, a facile solution-processed room-temperature method was developed to fabricate a new CsPbBr₃-Co₃O₄ heterojunction photocatalyst for visible-light-driven CO₂ conversion. The successful formation of the CsPbBr₃-Co₃O₄ hybrid was confirmed by XRD, TEM, HRTEM and XPS analysis. The enhanced generation of CO (35.40 μmol g⁻¹ h⁻¹) and CH₄ (29.2 μmol g⁻¹ h⁻¹) with a high *R*_{electron} rate (304.4 μmol g⁻¹ h⁻¹) was realized on the CsPbBr₃-Co₃O₄ hybrid, which outperformed the counter products and some state-of-the-art photocatalysts. The formation of staggered band alignment and an intimately contacted heterointerface led to robust separation and directional transfer of charge carriers. Because of the uninterrupted flow of reductive e⁻, an electron enrichment zone was obtained at the active site of Co₃O₄, which ensured the efficient conversion of CO₂. This work describes the potential of designing a new perovskite-based heterojunction that could enable efficient charge separation to achieve better solar-driven CO₂ conversion.

Author contributions

Xin Zhong: methodology, investigation, data curation, and writing the original draft. Xinmeng Liang: methodology, investigation, data curation, and writing the original draft. Xinyu Lin: methodology, investigation, and validation. Malik Zeeshan Shahid: writing the original draft, visualization, investigation, and data curation. Jin Wang: supervision, conceptualization, descriptions, and funding acquisition. Zhengquan Li: supervision, conceptualization, descriptions, and funding acquisition.

Conflicts of interest

There are no conflicts to declare.

Acknowledgements

This work was financially supported by the National Natural Science Foundation of China (21701143, 21975223), the Natural Science Foundation of Zhejiang Province (LGG19B010002, LZ22B030002), and the Industrial Key Projects of Jinhua City (2021A22383).

References

- 1 J. Wang, Y. Shi, Y. Wang and Z. Li, Rational design of metal halide perovskite nanocrystals for photocatalytic CO₂ reduction: Recent advances, challenges, and prospects, *ACS Energy Lett.*, 2022, 7, 2043–2059.
- 2 S. Yin, X. Zhao, E. Jiang, Y. Yan, P. Zhou and P. Huo, Boosting water decomposition by sulfur vacancies for efficient CO₂ photoreduction, *Energy Environ. Sci.*, 2022, 15, 1556–1562.
- 3 Y. Feng, C. Wang, P. Cui, C. Li, B. Zhang, L. Gan, S. Zhang, X. Zhang, X. Zhou, Z. Sun, K. Wang, Y. Duan, H. Li, K. Zhou, H. Huang, A. Li, C. Zhuang, L. Wang, Z. Zhang and X. Han, Ultrahigh photocatalytic CO₂ reduction efficiency and selectivity manipulation by single-tungsten-atom oxide at the atomic step of TiO₂, *Adv. Mater.*, 2022, 34, 2109074.
- 4 J. Wang, L. Xiong, Y. Bai, Z. J. Chen, Q. Zheng, Y. Y. Shi, C. Zhang, G. C. Jiang and Z. Q. Li, Mn-doped perovskite nanocrystals for photocatalytic CO₂ reduction: Insight into the role of the charge carriers with prolonged lifetime, *Sol. RRL*, 2022, 6, 2200294.
- 5 S. Xu, Q. Shen, J. Zheng, Z. Wang, X. Pan, N. Yang and G. Zhao, Advances in biomimetic photoelectrocatalytic reduction of carbon dioxide, *Adv. Sci.*, 2022, 2203941.
- 6 S. H. Teo, C. H. Ng, Y. H. Ng, A. Islam, S. Hayase and Y. H. Taufiq-Yap, Resolve deep-rooted challenges of halide perovskite for sustainable energy development and environmental remediation, *Nano Energy*, 2022, 99, 107401.
- 7 E. Gong, S. Ali, C. B. Hiragond, H. S. Kim, N. S. Powar, D. Kim, H. Kim and S.-I. In, Solar fuels: research and development strategies to accelerate photocatalytic CO₂ conversion into hydrocarbon fuels, *Energy Environ. Sci.*, 2022, 15, 880–937.
- 8 Y. Wang, E. Chen and J. Tang, Insight on reaction pathways of photocatalytic CO₂ conversion, *ACS Catal.*, 2022, 12, 7300–7316.
- 9 Ž. Kovačič, B. Likozar and M. Huš, Photocatalytic CO₂ reduction: A review of Ab initio mechanism, kinetics, and multiscale modeling simulations, *ACS Catal.*, 2020, 10, 14984–15007.

- 10 H. Bian, D. Li, S. Wang, J. Yan and S. F. Liu, 2D-C₃N₄ encapsulated perovskite nanocrystals for efficient photo-assisted thermocatalytic CO₂ reduction, *Chem. Sci.*, 2022, **13**, 1335–1341.
- 11 S. D. Yang, H. Y. Li, H. M. Li, H. M. Li, W. S. Qi, Q. Zhang, J. Zhu, P. Zhao and L. Chen, Rational design of 3D carbon nitrides assemblies with tunable nano-building blocks for efficient visible-light photocatalytic CO₂ conversion, *Appl. Catal., B*, 2022, **316**, 121612.
- 12 M. Gao, J. Zhang, P. Zhu, X. Liu and Z. Zheng, Unveiling the origin of alkali metal promotion in CO₂ methanation over Ru/ZrO₂, *Appl. Catal., B*, 2022, **314**, 121476.
- 13 L. Collado, P. Reñones, J. Fermoso, F. Fresno, L. Garrido, V. Pérez-Dieste, C. Escudero, M. D. Hernández-Alonso, J. M. Coronado, D. P. Serrano and V. A. D. O'Shea, The role of the surface acidic/basic centers and redox sites on TiO₂ in the photocatalytic CO₂ reduction, *Appl. Catal., B*, 2022, **303**, 120931.
- 14 S. Wei, Q. Heng, Y. Wu, W. Chen, X. Li and W. Shangguan, Improved photocatalytic CO₂ conversion efficiency on Ag loaded porous Ta₂O₅, *Appl. Surf. Sci.*, 2021, **563**, 150273.
- 15 X. Lin, S. Xia, L. Zhang, Y. Zhang, S. Sun, Y. Chen, S. Chen, B. Ding, J. Yu and J. Yan, Fabrication of flexible mesoporous black Nb₂O₅ nanofiber films for visible-light-driven photocatalytic CO₂ Reduction into CH₄, *Adv. Mater.*, 2022, **34**, 2200756.
- 16 J. Wang, S. Lin, N. Tian, T. Ma, Y. Zhang and H. Huang, Nanostructured metal sulfides: classification, modification strategy, and solar-driven CO₂ reduction application, *Adv. Funct. Mater.*, 2020, **31**, 2008008.
- 17 C. I. Ezugwu, S. Liu, C. Li, S. Zhuiykov, S. Roy and F. Verpoort, Engineering metal-organic frameworks for efficient photocatalytic conversion of CO₂ into solar fuels, *Coord. Chem. Rev.*, 2022, **450**, 214245.
- 18 C. B. Hiragond, N. S. Powar, J. Lee and S. I. In, Single-atom catalysts (SACs) for photocatalytic CO₂ reduction with H₂O: activity, product selectivity, stability, and surface chemistry, *Small*, 2022, **18**, 2201428.
- 19 X. J. Liu, T. Q. Chen, Y. H. Xue, J. C. Fan, S. L. Shen, M. S. A. A. Hossain, M. A. Amin, L. K. Pan, X. T. Xu and Y. Yamauchi, Nanoarchitectonics of MXene/semiconductor heterojunctions toward artificial photosynthesis via photocatalytic CO₂ reduction, *Coord. Chem. Rev.*, 2022, **459**, 214440.
- 20 S.-H. Wang, F. Khurshid, P.-Z. Chen, Y.-R. Lai, C.-W. Cai, P.-W. Chung, M. Hayashi, R.-J. Jeng, S.-P. Rwei and L. Wang, Solution-processable naphthalene diimide-based conjugated polymers as organocatalysts for photocatalytic CO₂ reaction with extremely stable catalytic activity for over 330 hours, *Chem. Mater.*, 2022, **34**, 4955–4963.
- 21 S. Chen, H. Yin, P. Liu, Y. Wang and H. Zhao, Stabilisation and performance enhancement strategies for halide perovskite photocatalysts, *Adv. Mater.*, 2022, **35**, 2203836.
- 22 H. Huang, D. Verhaeghe, B. Weng, B. Ghosh, H. Zhang, J. Hofkens, J. A. Steele and M. B. J. Roelofs, Metal halide perovskite based heterojunction photocatalysts, *Angew. Chem., Int. Ed.*, 2022, **61**, e202203261.
- 23 S. Purohit, K. L. Yadav and S. Satapathi, Metal halide perovskite heterojunction for photocatalytic hydrogen generation: progress and future opportunities, *Adv. Mater. Interfaces*, 2022, **9**, 2200058.
- 24 L. Y. Wu, Y. F. Mu, X. X. Guo, W. Zhang, Z. M. Zhang, M. Zhang and T. B. Lu, Encapsulating perovskite quantum dots in iron-based metal-organic frameworks (MOFs) for efficient photocatalytic CO₂ reduction, *Angew. Chem., Int. Ed.*, 2019, **58**, 9491–9495.
- 25 X. Zhu, L. Ge, Y. Wang, M. Li, R. Zhang, M. Xu, Z. Zhao, W. Lv and R. Chen, Recent advances in enhancing and enriching the optical properties of Cl-based CsPbX₃ nanocrystals, *Adv. Opt. Mater.*, 2021, **9**, 2100058.
- 26 M. Ou, W. Tu, S. Yin, W. Xing, S. Wu, H. Wang, S. Wan, Q. Zhong and R. Xu, Amino-assisted anchoring of CsPbBr₃ perovskite quantum dots on porous g-C₃N₄ for enhanced photocatalytic CO₂ reduction, *Angew. Chem., Int. Ed.*, 2018, **57**, 13570–13574.
- 27 M. Madi, M. Tahir and S. Tasleem, Advances in structural modification of perovskite semiconductors for visible light assisted photocatalytic CO₂ reduction to renewable solar fuels: A review, *J. Environ. Chem. Eng.*, 2021, **9**, 106264.
- 28 Y. F. Mu, W. Zhang, X. X. Guo, G. X. Dong, M. Zhang and T. B. Lu, Water-tolerant lead halide perovskite nanocrystals as efficient photocatalysts for visible-light-driven CO₂ reduction in pure water, *ChemSusChem*, 2019, **12**, 4769–4774.
- 29 L. Clinckemalie, D. Valli, M. B. J. Roelofs, J. Hofkens, B. Pradhan and E. Debroye, Challenges and opportunities for CsPbBr₃ perovskites in low- and high-energy radiation detection, *ACS Energy Lett.*, 2021, **6**, 1290–1314.
- 30 J. Wang, J. Liu, Z. Du and Z. Li, Recent advances in metal halide perovskite photocatalysts: Properties, synthesis and applications, *J. Energy Chem.*, 2021, **54**, 770–785.
- 31 G. Gao, Q. Xi, H. Zhou, Y. Zhao, C. Wu, L. Wang, P. Guo and J. Xu, Novel inorganic perovskite quantum dots for photocatalysis, *Nanoscale*, 2017, **9**, 12032–12038.
- 32 Q. A. Akkerman, T. P. T. Nguyen, S. C. Boehme, F. Montanarella, D. N. Dirin, P. Wechsler, F. Beiglbock, G. Raino, R. Erni, C. Katan, J. Even and M. V. Kovalenko, Controlling the nucleation and growth kinetics of lead halide perovskite quantum dots, *Science*, 2022, **377**, 1406–1412.
- 33 Z. Zhang, L. Li, Y. Jiang and J. Xu, Step-scheme photocatalyst of CsPbBr₃ quantum dots/BiOBr nanosheets for efficient CO₂ Photoreduction, *Inorg. Chem.*, 2022, **61**, 3351–3360.
- 34 X. Y. Yue, L. Cheng, J. J. Fan and Q. J. Xiang, 2D/2D BiVO₄/CsPbBr₃ S-scheme heterojunction for photocatalytic CO₂ reduction: Insights into structure regulation and Fermi level modulation, *Appl. Catal., B*, 2022, **304**, 120979.
- 35 C. C. Lin, T. R. Liu, S. R. Lin, K. M. Boopathi, C. H. Chiang, W. Y. Tzeng, W. C. Chien, H. S. Hsu, C. W. Luo, H. Y. Tsai, H. A. Chen, P. C. Kuo, J. Shiue, J. W. Chiou, W. F. Pong,

- C. C. Chen and C. W. Chen, Spin-polarized photocatalytic CO₂ reduction of Mn-Doped perovskite nanoplates, *J. Am. Chem. Soc.*, 2022, **144**, 15718–15726.
- 36 Q. Wang, J. Wang, J. C. Wang, X. Hu, Y. Bai, X. Zhong and Z. Li, Coupling CsPbBr₃ quantum dots with covalent triazine frameworks for visible-light-driven CO₂ reduction, *ChemSusChem*, 2021, **14**, 1131–1139.
 - 37 L. Ding, B. Borjigin, Y. Li, X. Yang, X. Wang and H. Li, Assembling an affinal 0D CsPbBr₃/2D CsPb₂Br₅ architecture by synchronously in situ growing CsPbBr₃ QDs and CsPb₂Br₅ nanosheets: enhanced activity and reusability for photocatalytic CO₂ reduction, *ACS Appl. Mater. Interfaces*, 2021, **13**, 51161–51173.
 - 38 J. Wang, J. Wang, N. Li, X. Du, J. Ma, C. He and Z. Li, Direct Z-scheme 0D/2D heterojunction of CsPbBr₃ quantum Dots/Bi₂WO₆ nanosheets for efficient photocatalytic CO₂ reduction, *ACS Appl. Mater. Interfaces*, 2020, **12**, 31477–31485.
 - 39 Y. Jiang, H. Y. Chen, J. Y. Li, J. F. Liao, H. H. Zhang, X. D. Wang and D. B. Kuang, Z-Scheme 2D/2D heterojunction of CsPbBr₃/Bi₂WO₆ for improved photocatalytic CO₂ reduction, *Adv. Funct. Mater.*, 2020, **30**, 2004293.
 - 40 Z. J. Chen, Y. G. Hu, J. Wang, Q. Shen, Y. H. Zhang, C. Ding, Y. Bai, G. C. Jiang, Z. Q. Li and N. Gaponik, Boosting photocatalytic CO₂ reduction on CsPbBr₃ perovskite nanocrystals by immobilizing metal complexes, *Chem. Mater.*, 2020, **32**, 1517–1525.
 - 41 S. Wan, M. Ou, Q. Zhong and X. Wang, Perovskite-type CsPbBr₃ quantum dots/Uio-66(NH₂) nanojunction as efficient visible-light-driven photocatalyst for CO₂ reduction, *Chem. Eng. J.*, 2019, **358**, 1287–1295.
 - 42 Z.-C. Kong, J.-F. Liao, Y.-J. Dong, Y.-F. Xu, H.-Y. Chen, D.-B. Kuang and C.-Y. Su, Core@Shell CsPbBr₃@Zeolitic imidazolate framework nanocomposite for efficient photocatalytic CO₂ reduction, *ACS Energy Lett.*, 2018, **3**, 2656–2662.
 - 43 Y. F. Xu, M. Z. Yang, B. X. Chen, X. D. Wang, H. Y. Chen, D. B. Kuang and C. Y. Su, A CsPbBr₃ perovskite quantum dot/Graphene oxide composite for photocatalytic CO₂ reduction, *J. Am. Chem. Soc.*, 2017, **139**, 5660–5663.
 - 44 Q. Zhang, P. Yang, H. Zhang, J. Zhao, H. Shi, Y. Huang and H. Yang, Oxygen vacancies in Co₃O₄ promote CO₂ photoreduction, *Appl. Catal., B*, 2022, **300**, 120729.
 - 45 Z. Feng, X. Zhu, J. Yang, K. Zhong, Z. Jiang, Q. Yu, Y. Song, Y. Hua, H. Li and H. Xu, Inherent facet-dominant effect for cobalt oxide nanosheets to enhance photocatalytic CO₂ reduction, *Appl. Surf. Sci.*, 2022, **578**, 151848.
 - 46 P. Yang, Q. Zhang, Z. Yi, J. Wang and H. Yang, Rational electronic control of carbon dioxide reduction over cobalt oxide, *J. Catal.*, 2020, **387**, 119–128.
 - 47 L. Huang, B. Li, B. Su, Z. Xiong, C. Zhang, Y. Hou, Z. Ding and S. Wang, Fabrication of hierarchical Co₃O₄@CdIn₂S₄ p–n heterojunction photocatalysts for improved CO₂ reduction with visible light, *J. Mater. Chem. A*, 2020, **8**, 7177–7183.
 - 48 L. Wang, J. Wan, Y. Zhao, N. Yang and D. Wang, Hollow multi-shelled structures of Co₃O₄ dodecahedron with unique crystal orientation for enhanced photocatalytic CO₂ reduction, *J. Am. Chem. Soc.*, 2019, **141**, 2238–2241.
 - 49 J. Y. Choi, C. K. Lim, B. Park, M. Kim, A. Jamal and H. Song, Surface activation of cobalt oxide nanoparticles for photocatalytic carbon dioxide reduction to methane, *J. Mater. Chem. A*, 2019, **7**, 15068–15072.
 - 50 W. Chen, B. Han, C. Tian, X. Liu, S. Liang, H. Deng and Z. Lin, MOFs-derived ultrathin holey Co₃O₄ nanosheets for enhanced visible light CO₂ reduction, *Appl. Catal., B*, 2019, **244**, 996–1003.
 - 51 X. Huang, Q. Shen, J. Liu, N. Yang and G. Zhao, A CO₂ adsorption-enhanced semiconductor/metal-complex hybrid photoelectrocatalytic interface for efficient formate production, *Energy Environ. Sci.*, 2016, **9**, 3161–3171.
 - 52 C. Gao, Q. Meng, K. Zhao, H. Yin, D. Wang, J. Guo, S. Zhao, L. Chang, M. He, Q. Li, H. Zhao, X. Huang, Y. Gao and Z. Tang, Co₃O₄ Hexagonal platelets with controllable facets enabling highly efficient visible-light photocatalytic reduction of CO₂, *Adv. Mater.*, 2016, **28**, 6485–6490.
 - 53 L. Wang, J. Deng, Z. Lou and T. Zhang, Nanoparticles-assembled Co₃O₄ nanorods p-type nanomaterials: One-pot synthesis and toluene-sensing properties, *Sens. Actuators, B*, 2014, **201**, 1–6.
 - 54 L. Li, C. Zhang, R. Zhang, X. Gao, S. He, M. Liu, X. Li and W. Chen, 2D ultrathin Co₃O₄ nanosheet array deposited on 3D carbon foam for enhanced ethanol gas sensing application, *Sens. Actuators, B*, 2017, **244**, 664–672.
 - 55 A. Aljabour, H. Coskun, D. H. Apaydin, F. Ozel, A. W. Hassel, P. Stadler, N. S. Sariciftci and M. Kus, Nanofibrous cobalt oxide for electrocatalysis of CO₂ reduction to carbon monoxide and formate in an acetonitrile-water electrolyte solution, *Appl. Catal., B*, 2018, **229**, 163–170.
 - 56 Y. Gu, J. Ding, X. Tong, H. Yao, R. Yang and Q. Zhong, Photothermal catalyzed hydrogenation of carbon dioxide over porous nanosheet Co₃O₄, *J. CO₂ Util.*, 2022, **61**, 102003.
 - 57 X. Zhu, H. Ji, J. Yi, J. Yang, X. She, P. Ding, L. Li, J. Deng, J. Qian, H. Xu and H. Li, A specifically exposed cobalt oxide/carbon nitride 2D heterostructure for carbon dioxide photoreduction, *Ind. Eng. Chem. Res.*, 2018, **57**, 17394–17400.
 - 58 W. Yang, G. Ma, Y. Fu, K. Peng, H. Yang, X. Zhan, W. Yang, L. Wang and H. Hou, Rationally designed Ti₃C₂ MXene@TiO₂/CuInS₂ Schottky/S-scheme integrated heterojunction for enhanced photocatalytic hydrogen evolution, *Chem. Eng. J.*, 2022, **429**, 132381.
 - 59 X.-T. Liu, B.-H. Li, X.-J. Wang, Y.-L. Li, J. Zhao, Y.-P. Li and F.-T. Li, Enhanced schottky effect in the Ni₂P cocatalyst via work function up-shift induced by MoO₂ for boosting photocatalytic hydrogen evolution, *ACS Sustainable Chem. Eng.*, 2022, **10**, 10627–10640.
 - 60 K. Liu, H. Zhang, T. Fu, L. Wang, R. Tang, Z. Tong and X. Huang, Construction of BiOBr/Ti₃C₂/exfoliated montmorillonite Schottky junction: New insights into exfoliated montmorillonite for inducing MXene oxygen functional-

- zation and enhancing photocatalytic activity, *Chem. Eng. J.*, 2022, **438**, 135609.
- 61 Y. Li, Q. Zhao, Y. Zhang, Y. Li, L. Fan, F.-T. Li and X. Li, In-situ construction of sequential heterostructured CoS/CdS/CuS for building “electron-welcome zone” to enhance solar-to-hydrogen conversion, *Appl. Catal., B*, 2022, **300**, 120763.
 - 62 J. Li, L. Xu, T. Wang, J. Song, J. Chen, J. Xue, Y. Dong, B. Cai, Q. Shan, B. Han and H. Zeng, 50-Fold EQE Improvement up to 6.27% of solution-processed all-inorganic perovskite CsPbBr₃ QLEDs via surface ligand density control, *Adv. Mater.*, 2017, **29**, 1603885.
 - 63 N. Li, X. Chen, J. Wang, X. Liang, L. Ma, X. Jing, D. L. Chen and Z. Li, ZnSe Nanorods-CsSnCl₃ perovskite heterojunction composite for photocatalytic CO₂ reduction, *ACS Nano*, 2022, **16**, 3332–3340.
 - 64 D. Barreca, C. Massignan, S. Daolio, M. Fabrizio, C. Piccirillo, L. Armelao and E. Tondello, Composition and microstructure of cobalt oxide thin films obtained from a novel cobalt(II) precursor by chemical vapor deposition, *Chem. Mater.*, 2001, **13**, 588–593.
 - 65 Z. Hu, L. Hao, F. Quan and R. Guo, Recent developments of Co₃O₄-based materials as catalysts for the oxygen evolution reaction, *Catal. Sci. Technol.*, 2022, **12**, 436–461.
 - 66 Y. Xu, F. Zhang, T. Sheng, T. Ye, D. Yi, Y. Yang, S. Liu, X. Wang and J. Yao, Clarifying the controversial catalytic active sites of Co₃O₄ for the oxygen evolution reaction, *J. Mater. Chem. A*, 2019, **7**, 23191–23198.
 - 67 W. He, L. Liu, T. Ma, H. Han, J. Zhu, Y. Liu, Z. Fang, Z. Yang and K. Guo, Controllable morphology CoFe₂O₄/g-C₃N₄ p-n heterojunction photocatalysts with built-in electric field enhance photocatalytic performance, *Appl. Catal., B*, 2022, **306**, 121107.
 - 68 S. Bai, J. Jiang, Q. Zhang and Y. Xiong, Steering charge kinetics in photocatalysis: intersection of materials syntheses, characterization techniques and theoretical simulations, *Chem. Soc. Rev.*, 2015, **44**, 2893–2939.